Water Supply

Water Supply Vol 22 No 4, 4109 doi: 10.2166/ws.2022.036

Modeling bulk surface resistance and evaluation of evapotranspiration using remote sensing and MATLAB

N. C. Sanjay Shekar [a,*] and B. C. Kumar Raju[b]

[a] Department of Civil Engineering, JSS Academy of Technical Education, Bangalore, Karnataka, India
[b] Department of Civil Engineering, Sapthagiri College of Engineering, Bangalore, Karnataka, India
*Corresponding author. E-mail: sanjayshekarnc@jssateb.ac.in

NCSS, 0000-0003-2817-8276

ABSTRACT

In developing countries, computation of actual evapotranspiration (AET) is challenging due to the lack of ground-based flux measurement data. The estimation of AET is crucial for water resources management involving the allocation of water for different land use/land cover (LULC) classes. The study's novelty was mapping pixel-by-pixel spatial variations of bulk surface resistance and evaluating the derived actual evapotranspiration in a sub-humid tropical river basin where flux tower data was lacking for validation. This study aimed to map bulk surface resistance and evaluate the estimated AET by global evapotranspiration data product (MOD16A2). Moderate Resolution Imaging Spectroradiometer (MODIS) data products, including land surface reflectance (LSR), land surface temperature (LST) and leaf area index (LAI) data, were used as input in MATLAB for mapping pixel-wise variations to analyze the seasonal variations in bulk surface resistance (r_s) and AET in pre-monsoon and post-monsoon seasons during the years 2019 and 2012. The years 2019 and 2012 were selected because 2019 experienced a relatively wet pre-monsoon and post-monsoon, whereas 2012 experienced the opposite conditions, which proved useful when interpreting variations that are influenced by wetness conditions. Overall, the results indicated significant variability in the r_s and AET for different LULC classes. MOD16A2 AET was determined to be slightly higher than the LULC classes' estimated AET. This study's MODIS satellite data products provided information on surface characteristics at a reasonable resolution. This permitted the identification of differences in LULC classes and changes in surface characteristics by season and wetness conditions, which are helpful when estimating AET.

Key words: actual evapotranspiration, bulk surface resistance, MATLAB, remote sensing

HIGHLIGHT

- The study's novelty was mapping pixel-by-pixel spatial variations of bulk surface resistance and evaluating the derived actual evapotranspiration in a sub-humid tropical river basin where flux tower data was deficient for validation.

LIST OF ACRONYMS

Abbreviation	Description
A	Available Energy Flux
c_p	Specific Heat of the Air
D_a	Vapor Pressure Deficit
D_{50}	Vapour Pressure Deficit at Which Stomatal Conductance Is Half
e_a	Actual Vapor Pressure
e_s	Saturation Vapour Pressure
f	Ratio of Evaporation from Soil to the Equilibrium Evaporation Rate
G	Soil Heat Flux
g_{sx}	Maximum Stomatal Conductance
Ga	Aerodynamic Conductance
Gc	Bulk Canopy Conductance
Gs	Surface Conductance
Gi	Climatological Conductance

G_{daily}	Soil Heat Flux Integrated Over 24 hours
k_A	Extinction Coefficient for Available Energy
k_Q	Extinction Coefficient for Shortwave Radiation
Qh	Flux Density of Visible Radiation at the Top of Canopy
Q_{50}	Visible Radiation Flux when Stomatal Conductance is Half
r_a	Aerodynamic Resistance
r_s	Surface Resistance
RH	Relative Humidity
R_n	Net Radiation
$R_{n\ daily}$	Daily Average Net Radiation
Ta	Air Temperature
u_z	Wind Speed at Height z_m
γ	Psychometric Constant
λET	Latent Heat Flux
ρ_a	Mean Air Density
$\triangle$	Slope of Saturation Vapour Pressure Curve
τ	Fraction of Total Available Energy Absorbed by Soil Surface
λ	Latent Heat of Water
ρw	Density of Water
AET	Actual Evapotranspiration
ArcGIS	Aeronautical Reconnaissance Coverage Geographic Information System
DEM	Digital Elevation Model
EF	Evaporative Fraction
eqn	Equation
GIS	Geographic Information System
IMD	Indian Meteorological Department
LAI	Leaf Area Index Obtained from MODIS Remote Sensing
LISS	Linear Imaging Self-scanning Sensor
LSR	Land Surface Reflectance
LST	Corrected Land Surface Temperature
LULC	Land Use and Land Cover
MATLAB	MATric LABoratory
MODIS	Moderate Resolution Imaging Spectroradiometer
MOD11A2	Product of Land Surface Temperature
MOD09A1	Product of Land Surface Reflectance
MOD15A2	Product of Leaf Area Index
MOD16A2	Product for Global Terrestrial Evapotranspiration
MRT	MODIS Reprojection Tool
PML	Leuning *et al.* (2008) Bulk Surface Conductance Model
PM	Penman-Monteith
TIFF	Tag Image File Format

1. INTRODUCTION

Characterizing the spatial variabilities of actual evapotranspiration (AET) from heterogeneous landscapes is essential in hydrology, climate variability, agriculture, irrigation, water resources engineering and management as environmental impact assessments (Droogers *et al.* 2010; Minacapilli *et al.* 2016; Khaniya *et al.* 2020). AET combines two separate processes where moisture is lost from the soil surface by direct evaporation and via vegetation by transpiration. Furthermore, AET is a significant water balance component, sometimes accounting for over 60 percent of the annual water balance. Therefore, enhanced methods are required for the accurate computation of AET in a field to improve the efficient use of water resources and productivity (Hobbins *et al.* 2001; Howell 2001; Allen *et al.* 2007; Taylor *et al.* 2013).

Modeling AET is complex, and the direct measurement of AET in large basins can be challenging. The MODIS-based remote sensing technology, which can also provide estimates in ungauged areas where ground-based flux observations are unavailable, is one viable approach for computing regional AET. Numerous literature reviews have indicated that MODIS data products provide land use/land cover (LULC) characteristics information to estimate AET conveniently and cost-effectively. (e.g., Cleugh *et al.* 2007; Mu *et al.* 2007; Leuning *et al.* 2008; Zhang *et al.* 2009).

AET can be computed using the Penman-Monteith (PM) equation. Several researchers have proposed using remotely sensed data to estimate the daily AET using the PM approach at regional and global scales (Nagler *et al.* 2005; Mu *et al.*

2007; Leuning *et al.* 2008; Zhang *et al.* 2008; Guerschman *et al.* 2009). However, bulk surface resistance is a complex parameter influenced by numerous variables; estimating it when using the PM method is stimulating. Bulk surface resistance modeling has been the subject of intense research to develop a PM model. The global evapotranspiration data product was developed by Mu *et al.* (2007) based on the Cleugh *et al.* (2007) surface conductance model.

A study of the literature on evaluating the spatial pixel-wise AET estimates of global evapotranspiration data product (MOD16A2) was conducted and the results are summarised below. Ruhoff *et al.* (2013) used data from flow towers to estimate AET, then validated using the MGB-IPH hydrological model and MOD16A2 AET data. Cherif *et al.* (2015) compared the results to MOD16A2 with a remotely sensed SEBAL model to improve the accuracy of AET estimates. Finally, Ke *et al.* (2017) utilized a machine learning model to compute AET-based spatial estimates and compared to MOD16A2, the study found that the Landsat data fusion provided high accuracy for estimated AET.

It is evident from the literature review that several studies exist and have modeled surface resistance and AET using different data inputs, methodologies, algorithms, satellites, spatial scales and validation techniques in other climatic conditions (Li *et al.* 2016; Dimitriadou & Nikolakopoulos 2021; Mobilia & Longobardi 2021). However, most of the algorithms use satellite data combined with ground-based meteorological and flux data. Due to the lack of flux data for validation of the proposed model, the AET estimation was undertaken using the surface conductance model of Penman-Monteith integrated with Leuning *et al.* (2008) (PML), which requires satellite data with limited meteorological data inputs. Hence the objective of this study was to use satellite imagery with meteorological data inputs and MATLAB to map bulk surface resistance and evaluate the estimated AET by the MOD16A2.

2. STUDY AREA

On the Kaveri River's northern bank (Figure 1), the Hemavathi River is among the most important tributaries. It rises in the Western Ghats near Ballalara- Yanadurga in the Mudigere taluk of Chikmagalur district. The river basin is located between the North latitudes of 13°22′30″ to 12°35′15″ and the East longitudes of 75°31′30″ to 76°39′45″. The river joins the Cauvery River in the Krishnarajasagar Reservoir in Akkihebbal after a 245-kilometer. The Hemavathi River basin covers 5,427 square kilometers. From March through May, the pre-monsoon season begins. From June until October, the rainy season lasts. During the rainy season, extreme rainstorms are common. November through February are the post-monsoon months where the weather is quite cold. The investigation's catchment is hilly, with steep to moderate slopes. The slope is steeper at higher elevations and eventually decreases. Figure 1 shows the overall elevation of the basin, which ranges from 748 to 1,853 metres above sea level. Plantations and agriculture are the backbone of the basin's economy. The Western Ghat section to the west is exposed to the full effect of southwest monsoon winds. Temperatures rise gradually from January through April in most parts of the basin. As a result, winds rise over the Western Ghats, bringing rain to the region. The passing of depressions is associated with heavy to highly severe rainfall. From June through September, the wind blows from the southwest to the northeast, causing the southwest monsoon to storm. Except for the Palghat gap, through which the southwest winds blow, the Western Ghats form a continuous barrier. As a result, the southwest monsoon shifts its direction from north–east to south–west around the end of September. The maximum quantity of cloudiness persists during the receding monsoon season. The cloudiest month is July, while the least cloudy month is March. The Western Ghats partially covers the study area. As a result, there is a wide range of vegetative cover in this western region.

3. DATA USED

3.1. MODIS satellite data products

In this study, the MODIS satellite data products mounted on the Terra platform were used. The data can be freely downloaded from the website. The products used in this study included the MOD11A2 product of land surface temperature (LST), the MOD09A1 product of land surface reflectance (LSR), the MOD15A2 product of leaf area index (LAI) and the MOD16A2 product for global terrestrial evapotranspiration. MODIS data products were chosen based on post-monsoon seasons (November) and the pre-monsoon (April) of years 2012 and 2019.

Rainfall data (Table 1) were collected from the Indian Meteorological Department. Between 2012 and 2019, yearly rainfall ranged from a high of 2,165 mm to a low of 1,042 mm, with a 1,530 mm average. Compared to the year 2019, which had 2,165 mm of rainfall and a lower LST, the year 2012 had 1,042 mm of rainfall, which was less than the normal annual rainfall and had a high LST. The climate in the catchment region is typical monsoon climate. According to rainfall records, 2012

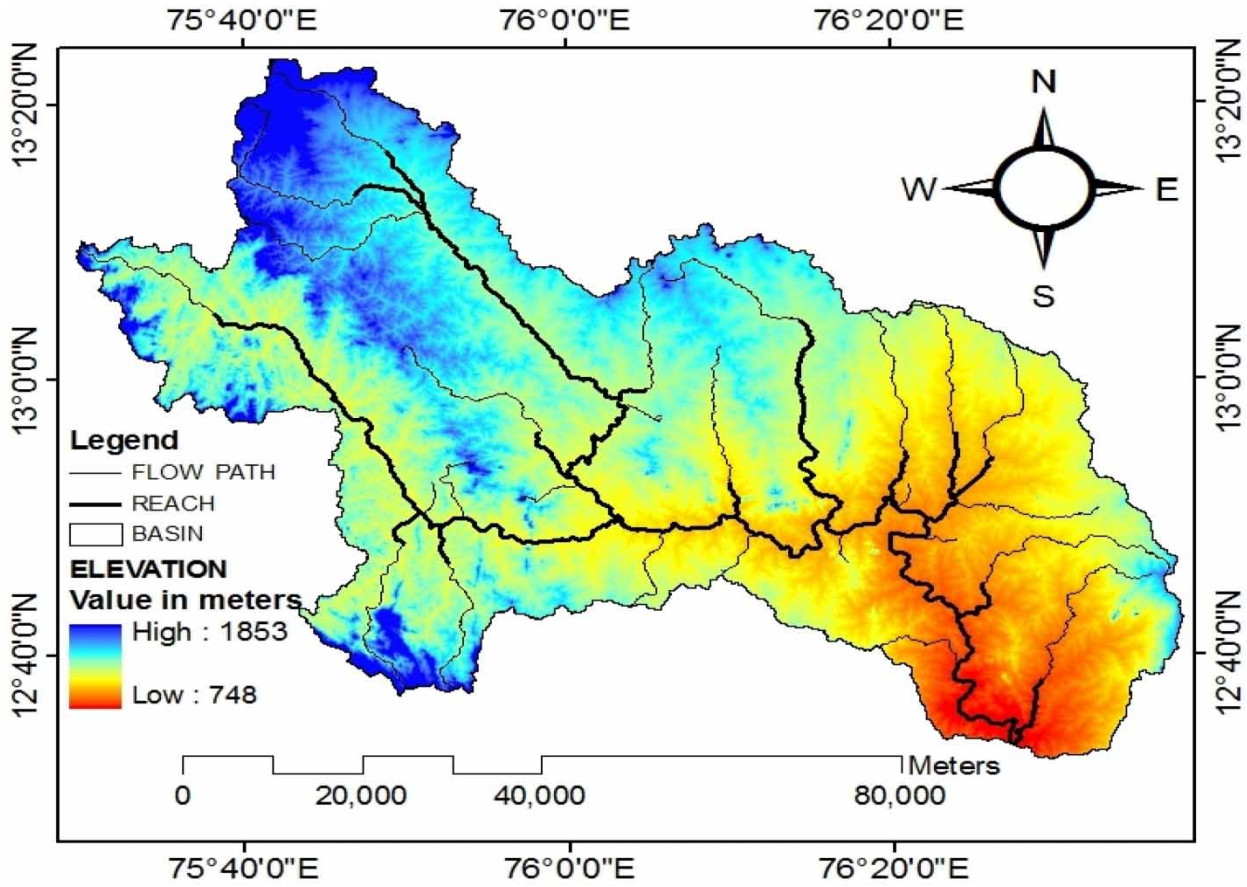

Figure 1 | Digital elevation model (DEM) of the study area.

Table 1 | Precipitation data of the study area

Years	Season	Rainfall (mm)	Annual Rainfall (mm)
2019	Pre-monsoon	562	2,165
	Post-monsoon	1,603	
2018	Pre-monsoon	575	1,824
	Post-monsoon	1,249	
2017	Pre-monsoon	496	1,469
	Post-monsoon	973	
2016	Pre-monsoon	556	1,541
	Post-monsoon	984	
2015	Pre-monsoon	403	1,392
	Post-monsoon	990	
2014	Pre-monsoon	514	1,580
	Post-monsoon	1,066	
2013	Pre-monsoon	438	1,228
	Post-monsoon	790	
2012	Pre-monsoon	341	1,042
	Post-monsoon	701	
Average Annual Rainfall			**1,530**

received significantly less rainfall both in pre-monsoon (dry condition) and post-monsoon (wet condition) than the annual average rainfall, while 2019 received significantly more rainfall both in pre-monsoon (dry condition) and post-monsoon (wet condition) than the annual average. As a result, these two years were chosen with care to study seasonal changes in LULC classes due to dry and wet moisture levels in pre-monsoon and post-monsoon seasons.

3.2. Land Use and land cover map

LULC data for the years 2012 and 2019 were taken from the Bhuvan website (https://bhuvan.nrsc.gov.in). The data utilized in this study was derived from Linear Imaging Self Scanning Sensor (LISS) - III data collected by the Resourcesat-1 satellite at a scale of 1:250,000. There are 19 classes (2nd level) in this data; however, only 14 land cover classes were found. The derived LULC map of the study area is shown in Figure 2. The existence of plantations may be observed in the basin's higher elevations (towards the west). However, agricultural crops and plantations were the most significant classes in the sub-humid tropical river basin.

4. METHODOLOGY

Figure 3 depicts the flow chart of steps involved in using the PM model proposed in this study to derive estimates of surface resistance and AET using inputs from MODIS imagery and meteorological data. First, pre-processing and post-processing of MODIS data products were undertaken using the MODIS Reprojection Tool (MRT), followed by the application of ArcGIS. Finally, all the necessary MODIS images were post-processed into TIFF formats for final processing in MATLAB. The flow-chart depicts the step-by-step procedure for estimating the variables, then describes the parameters in the following sections involved in computing surface resistance and AET using the PM approach.

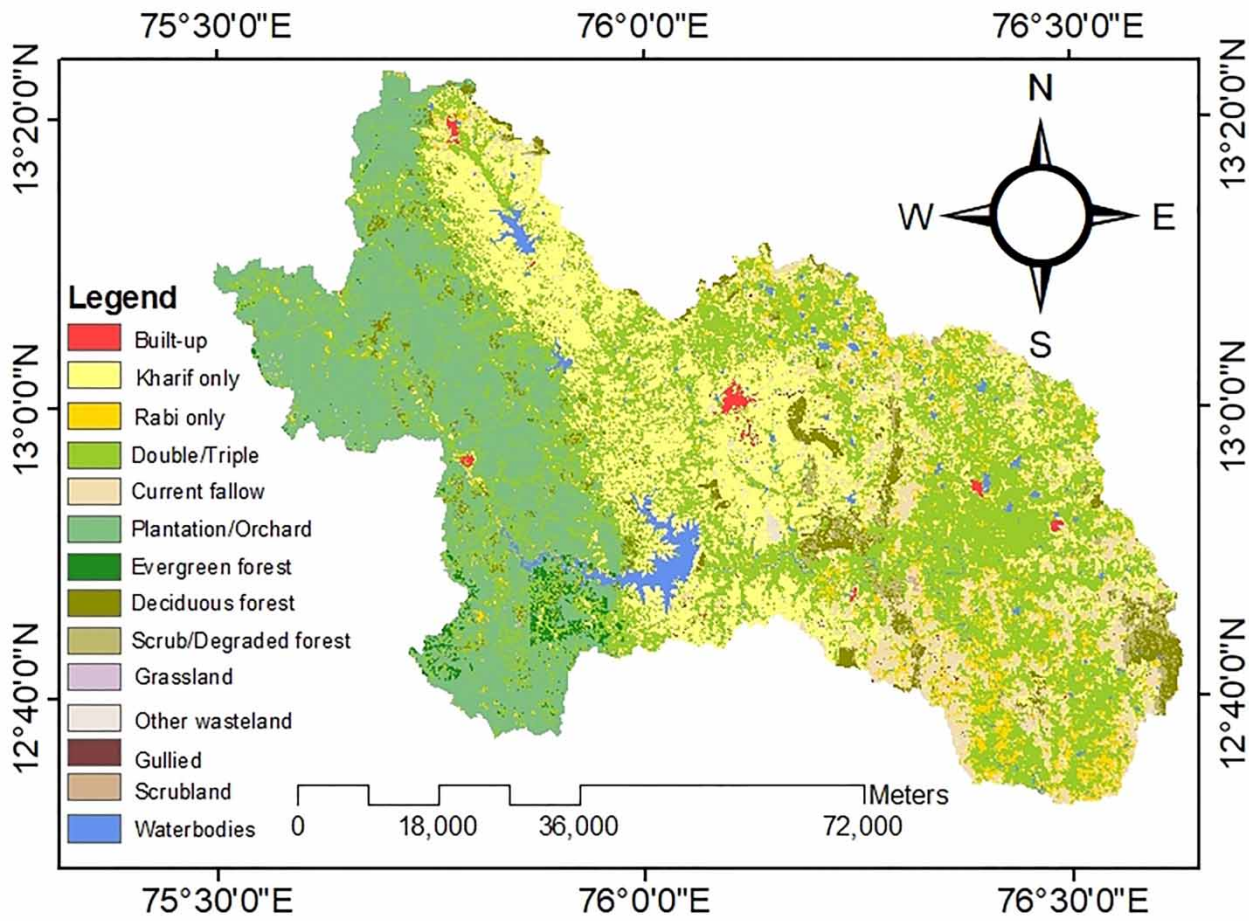

Figure 2 | Land cover classes in the Hemavathi River basin.

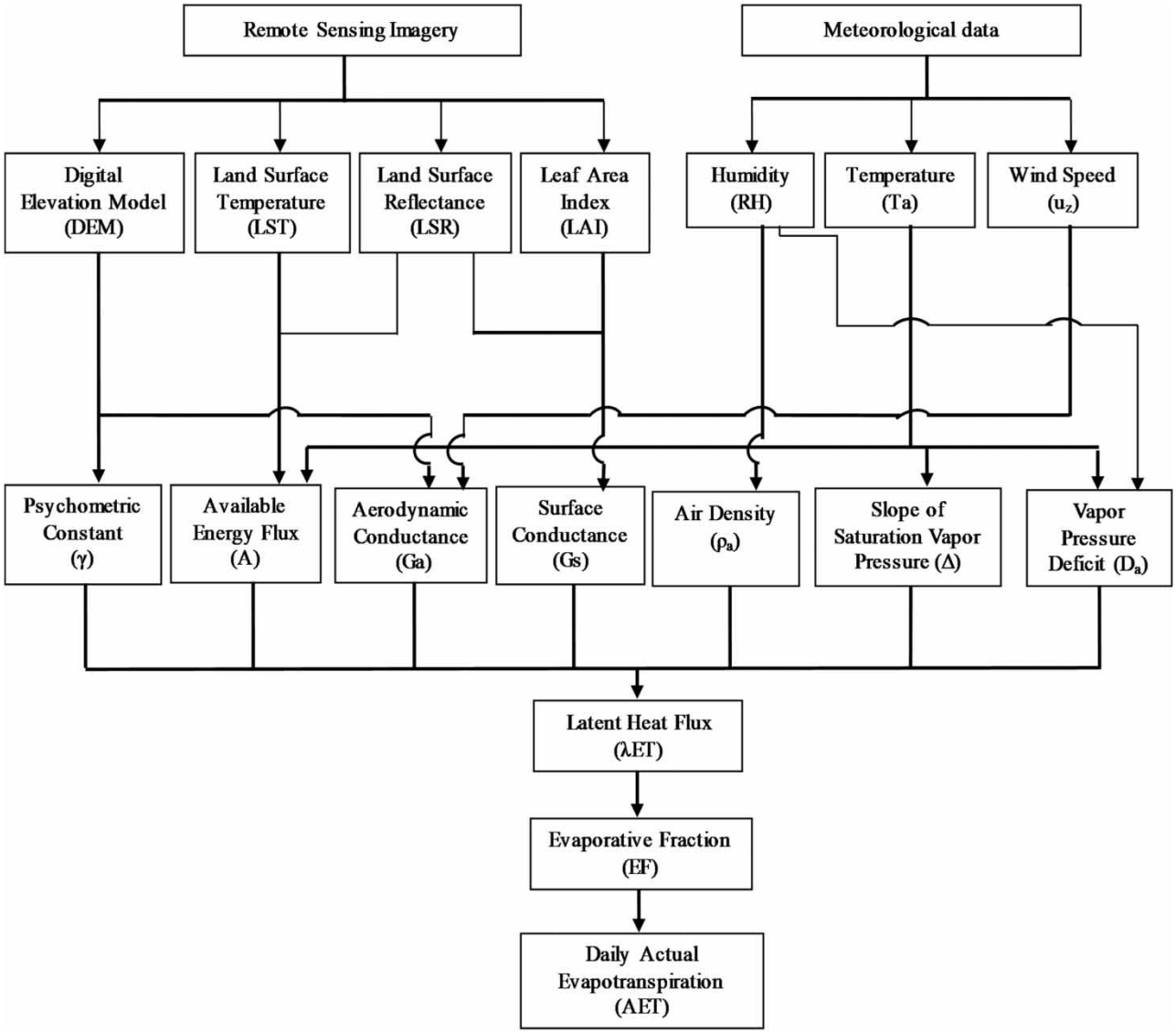

Figure 3 | Steps illustrating the estimation of AET using MATLAB.

4.1. Leuning *et al.* (2008) surface conductance (G_s) model

The pixelwise surface conductance (G_s) was estimated by the Leuning *et al.* (2008) surface conductance model, where (G_s) = $1/r_s$ by proposing a six parameters biophysical model (from now on referred to as PML) as given in Equations (1) and (2).

$$G_s = G_c \left[\frac{1 + \frac{\tau G_a}{\left(\frac{\Delta}{\gamma} + 1\right) G_c} \left[f - \frac{\left(\frac{\Delta}{\gamma} + 1\right)(1 - f) G_c}{G_a} \right] + \frac{G_a}{\frac{\Delta}{\gamma} G_i}}{1 - \tau \left[f - \frac{\left(\frac{\Delta}{\gamma} + 1\right)(1 - f) G_c}{G_a} \right] + \frac{G_a}{\frac{\Delta}{\gamma} G_i}} \right] \tag{1}$$

$$G_c = \frac{g_{sx}}{kQ} \ln \left[\frac{Q_h + Q50}{Q_h \exp(-kQ\ LAI) + Q50} \right] \left[\frac{1}{1 + \frac{Da}{D50}} \right] \tag{2}$$

where $\tau = \exp(-k_A\,LAI)$ and k_A = coefficient of extinction for energy available, LAI= leaf area index, Q_{50} =visible radiation flux at which stomatal conductance is half its maximum value (MJ/m^2/day), Q_h = visible radiation flux density at the top of canopy (MJ/m^2/day), k_Q= extinction coefficient for shortwave radiation, D_{50} = vapour pressure deficit when stomatal conductance is half its maximum value (kPa), D_a= vapour pressure deficit of air (kPa), g_{sx} = maximum stomatal conductance (m/s), G_c = bulk canopy conductance (m/s) and G_i = climatological conductance (m/s) i.e., $G_i = \gamma$ (Rn–G) /(ρacpDa).

As per the recommendations of Leuning *et al.* (2008), $k_A = k_Q = 0.6$, $Q_{50} = 30$ W/m^2 and $D_{50} = 0.7$ kPa values can be kept constant values across different LULC classes and optimization is required for only g_{sx} and f. According to Table 1 of Kelliher *et al.* (1995) the values of g_{sx} are fixed for the different LULC classes. The optimum value of f was determined by running the model algorithm where the values of f was varied from 0 to 1 in increments of 0.1 until the minimum RMSE was obtained between AET estimated.

4.2. The PM approach

The latent heat flux (λET) (W/m^2) is the energy used to evaporate the water that is estimated using the PM Equation (3) combined with a bulk surface resistance (r_s) which is estimated from LAI as the inverse of Gs. The PM equation is:

$$\lambda ET = \frac{[\Delta(R_n - G)] + \rho_a c_p \left(\frac{e_s - e_a}{r_a}\right)}{\Delta + \gamma\left[1 + \frac{r_s}{r_a}\right]} \tag{3}$$

where Δ =slope of saturation vapor pressure curve at air temperature (kPa/°C), which was calculated using Richards (1971), e_s and e_a = saturation and actual vapor pressure (kPa) of the air, which was computed using Allen *et al.* (2007), γ, ρ_a and c_p = psychrometric constant (kPa/°C), mean air density (kg/m^3) and specific heat of air (MJ/kg/°C), which was computed using, per Allen *et al.* (2007), R_n = net radiation (W/m^2), which was estimated using the procedures given by Allen *et al.* (2007), Bastiaanssen (2000) and Tasumi *et al.* (2003), G = soil heat flux (W/m^2), which was computed using Bastiaanssen (2000). r_s and r_a = the (bulk) surface and aerodynamic resistances (s/m), which were computed by combining the procedures given by Leuning *et al.* (2008). The terms Δ, e_s, e_a, ρ_a, r_a and γ were calculated using Cleugh *et al.* (2007).

4.3. Estimating AET

The instantaneous evaporative fraction (EF) Equation (4), (EF = Rn−G) is a ratio of latent heat flow values to accessible energy flux values. It's used to show how energy is partitioned in order to derive daily energy balance information from satellite data. The daily AET may be computed using EF and daily average net radiation data, according to Morse *et al.* (2000).

$$EF = \frac{\lambda ET}{R_n - G} \tag{4}$$

Due to the use of instantaneous satellite sensors to estimate all parameters, 24-hour AET is computed using Equation (5) assuming that EF remains constant due to latent heat of flow (Sugita & Brutsaert 1991).

$$AET_{daily} = \frac{8.64 \times 10^7 \times EF(R_{n\,daily} - G_{daily})}{\lambda \rho_w} \tag{5}$$

where λ = latent heat of water (2.47×10^6 kJ/kg) and, ρ_w = density of water (1,000 kg/m^3).

5. RESULTS AND DISCUSSION

As discussed earlier, the years 2012 and 2019 were selected for analysis as representative dry and wet years. These results with respect to antecedent rainfall conditions proved useful in the subsequent interpretation of differences in LULC characteristics and the influence of wetness conditions. Furthermore, implementing equations using satellite imagery yielded pixelwise values of r_s and AET across the Hemavathi River basin on pre-monsoon and post-monsoon days.

Figure 4 maps the bulk surface resistance variations derived from MATLAB with low average values observed post-monsoon compared to pre-monsoon for all the LULC classes due to the high moisture availibility with a high LAI. It can be

observed that high r_s values are likely where the LAI is low and has less moisture availability, limiting the AET process. Low r_s values are observed under high wetness and high LAI conditions, enhancing the AET. It can also be observed that the minimum values of r_s were lower for all LULC classes during the post-monsoon and pre-monsoon of 2019 (wet year) in comparison to the post-monsoon and pre-monsoon of 2012 (dry year). The r_s values also varied across the LULC classes with the lowest values calculated for the plantations and evergreen forest, which lies in the higher elevation towards the left side.

Table 2 shows the performance of the pixelwise AET values (5,427 pixels = 5,427 km^2) computed by the PML model compared to MOD16A2. For the LULC classes, the AET estimated by MOD16A2 was slightly higher than that estimated using the PML method. with an $R^2 = 0.78$ to 0.84 with a root mean square error (RMSE) = 0.39 to 0.48 mm/day and a bias (BIAS) = 0.13 to 0.18 mm/day for the post-monsoon and pre-monsoon seasons of years 2012 and 2019.

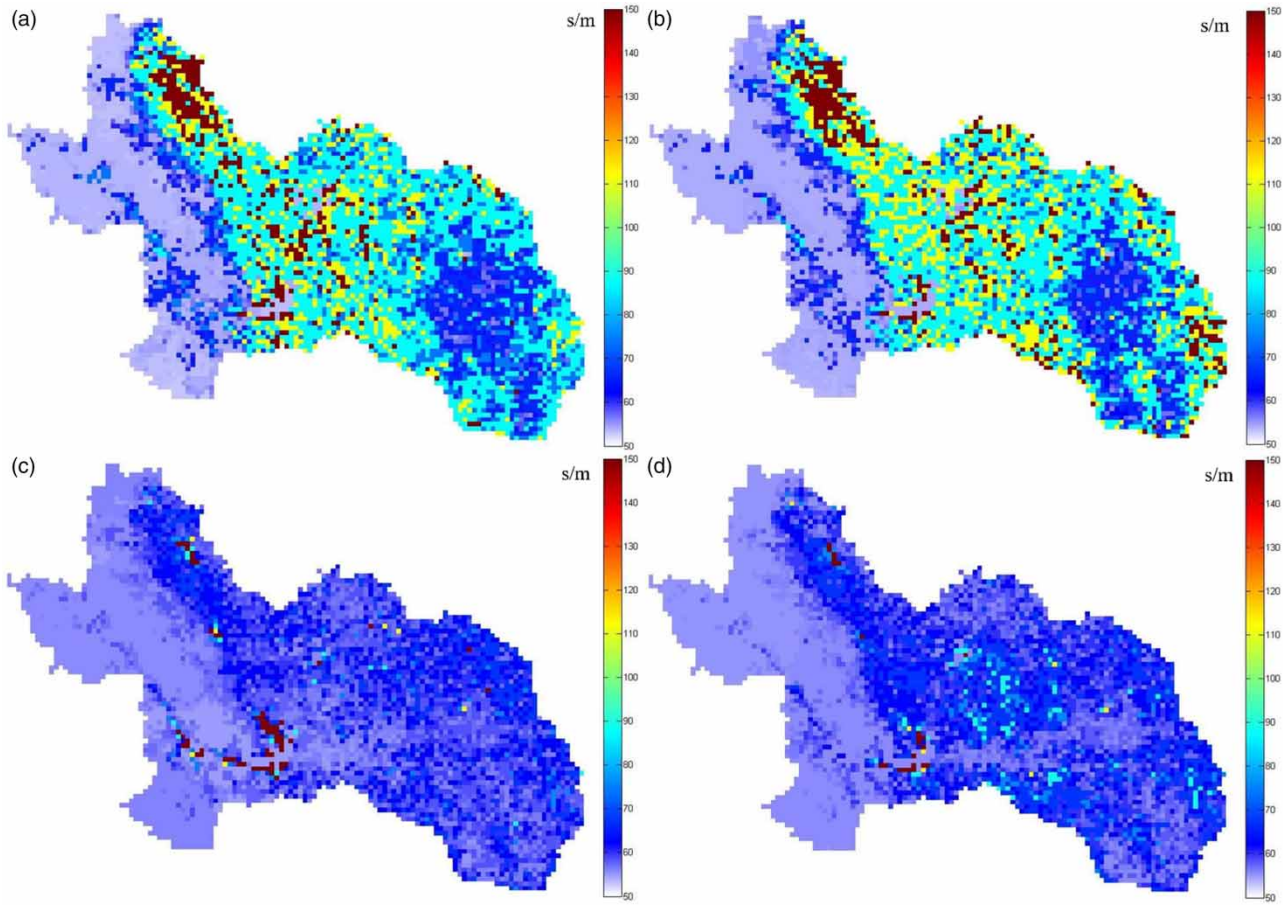

Figure 4 | Spatial variation of bulk surface resistance estimated by PML approach using MATLAB (a) Pre-monsoon, 2012 (b) Pre-monsoon, 2019 (c) Post-monsoon, 2012 (d) Post-monsoon, 2019.

Table 2 | Comparison of pixel-wise PML and MOD16A2 AET (mm/day) estimated using MATLAB

Season		R^2	RMSE (mm/day)	BIAS (mm/day)
2012	Pre-monsoon	0.83	0.45	0.13
	Post-monsoon	0.81	0.47	0.15
2019	Pre-monsoon	0.78	0.39	0.16
	Post-monsoon	0.84	0.48	0.18

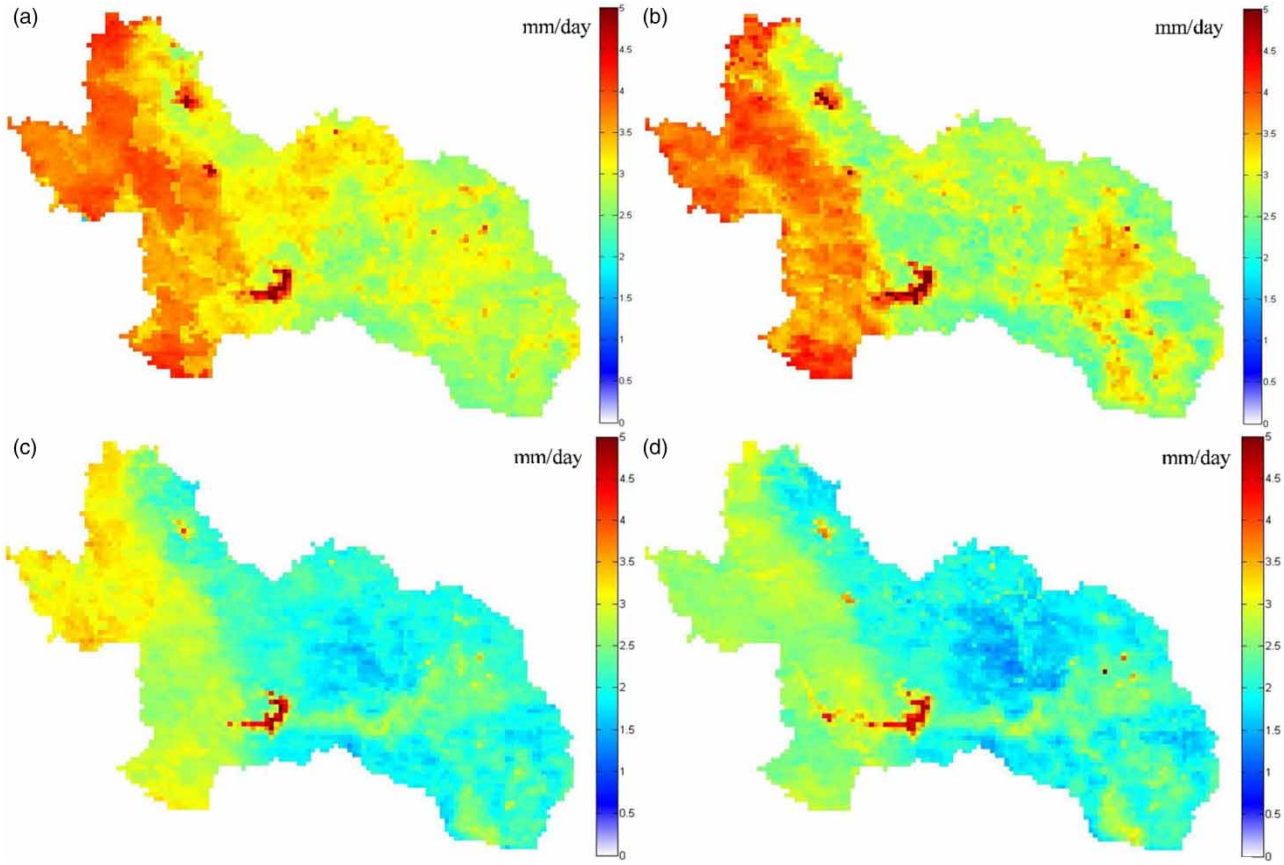

Figure 5 | Spatial variation of AET estimated by PML approach using MATLAB (a) Pre-monsoon, 2012 (b) Pre-monsoon, 2019 (c) Post-monsoon, 2012 (d) Post-monsoon, 2019.

Others (Ruhoff *et al.* 2013; Cherif *et al.* 2015; Autovino *et al.* 2016; Ke *et al.* 2017) found that MOD16A2 overestimated the AET (RMSE = 0.4–0.9 mm/day) when comparing spatial pixelwise AET estimations with MOD16A2 . Similarly, the AET estimated using MOD16A2 was found to be slightly higher than that estimated by the PML method in this investigation.

Figure 5 maps the daily evapotranspiration estimated using the PML approach in MATLAB, generated using AET pixelwise values. The variations in the AET were high and appeared to be related to wetness conditions and also the LULC class. As expected, the average AET values were low during the post-monsoon and high during the pre-monsoon. The ranking of the estimated AET was highest in waterbodies, followed by plantations, evergreen forest and grassland. It was found to be low in the gullied and other wastelands LULC classes. The topography, LULC, LST and moisture conditions influence the spatial distribution of AET variations across the basin. In both pre-monsoon and post-monsoon in 2012 and 2019, the AET at higher elevations of the basin was consistently higher than at lower elevations (see Figures 1 and 5). Due to high LST at the higher elevation, the average AET values are higher in pre-monsoon than post-monsoon in 2012 and 2019. For most classes, the AET in the post-monsoon of 2019 was slightly lower than in the post-monsoon of 2012 due to significantly less moisture in 2012 associated with reduced rainfall during the monsoon season.

6. CONCLUSIONS

The MODIS global evapotranspiration dataset was assessed and evaluated in the Hemavathi River Basin using the surface conductance model and MODIS satellite data products. The focus was on assessing the patterns of bulk surface resistance and evaluating the derived AET across different LULC classes present in the river basin. It was found that agricultural crops and plantations are the major classes in the basin. The analysis was undertaken in pre-monsoon and post-monsoon in 2012 (dry year) and 2019 (a wet year). The surface resistance and AET were computed for each pixel in the basin using MODIS-based satellite imagery products. Very high surface resistance values were observed under low wetness and low

LAI conditions. The variations in AET appeared to be related to wetness conditions, LST and the LULC class. Waterbodies had the highest AET losses estimated by the PML and MOD16A2 methods, followed by plantations, evergreen forest and grassland. For all the LULC classes, the AET estimated by MOD16A2 was slightly greater than that estimated using the PML method. It was concluded from the assessment that MODIS satellite data products provide information on the Earth's surface characteristics at a resolution that permits identification of not only differences in LULC classes but also on changes in these characteristics as a function of season, LST and moisture conditions. This work's developed methodology provided reasonably accurate regional/catchment scale surface resistance, AET estimations using satellite images and limited data inputs. Different satellite images with finer spatial resolution such as AVHRR and LANDSAT can be used to compare the performance of MODIS imagery. This will be critical in water balance investigations and hydrological models calibration.

ACKNOWLEDGEMENTS

The authors thank anonymous reviewers for giving tremendously valuable comments and suggestions to improve the quality of this manuscript, which are gratefully acknowledged.

DATA AVAILABILITY STATEMENT

All relevant data are included in the paper or its Supplementary Information.

REFERENCES

Allen, R. G., Tasumi, M., Morse, A., Trezza, R., Wright, J. L., Bastiaanssen, W., Kramber, W., Lorite, I. & Robison, C. W. 2007 Satellite-based energy balance for mapping evapotranspiration with internalized calibration (METRIC)–Applications. *Journal of Irrigation and Drainage Engineering* **133** (4), 395–406.

Autovino, D., Minacapilli, M. & Provenzano, G. 2016 Modelling bulk surface resistance by MODIS data and assessment of MOD16A2 evapotranspiration product in an irrigation district of Southern Italy. *Agricultural Water Management* **167**, 86–94.

Bastiaanssen, W. G. M. 2000 SEBAL-based sensible and latent heat fluxes in the Irrigated Gediz Basin, Turkey. *Journal of Hydrology* **229** (1–2), 87–100. doi:10.1016/S0022-1694(99)00202-4.

Cherif, I., Alexandridis, T. K., Jauch, E., Chambel-Leitao, P. & Almeida, C. 2015 Improving remotely sensed actual evapotranspiration estimation with raster meteorological data. *International Journal of Remote Sensing* **36** (18), 4606–4620.

Cleugh, H. A., Leuning, R., Mu, Q. & Running, S. W. 2007 Regional evaporation estimates from flux tower and MODIS satellite data. *Remote Sensing of Environment* **106** (3), 285–304.

Dimitriadou, S. & Nikolakopoulos, K. G. 2021 Annual actual evapotranspiration estimation via GIS models of three empirical methods employing remotely sensed data for the peloponnese, Greece, and comparison with annual MODIS ET and pan evaporation measurements. *ISPRS International Journal of Geo-Information* **10** (8), 522.

Droogers, P., Immerzeel, W. W. & Lorite, I. J. 2010 Estimating actual irrigation application by remotely sensed evapotranspiration observations. *Agricultural Water Management* **97** (9), 1351–1359.

Guerschman, J. P., Van Dijk, A. I., Mattersdorf, G., Beringer, J., Hutley, L. B., Leuning, R., Pipunic, R. C. & Sherman, B. S. 2009 Scaling of potential evapotranspiration with MODIS data reproduces flux observations and catchment water balance observations across Australia. *Journal of Hydrology* **369** (1–2), 107–119.

Hobbins, M. T., Ramírez, J. A., Brown, T. C. & Claessens, L. H. J. M. 2001 The complementary relationship in estimation of regional evapotranspiration: the complementary relationship areal evapotranspiration and advection-Aridity models. *Water Resources Research* **37** (5), 1367–1387.

Howell, T. A. 2001 Enhancing water use efficiency in irrigated agriculture. *Agronomy Journal* **93**, 281–289.

Ke, Y., Im, J., Park, S. & Gong, H. 2017 Spatiotemporal downscaling approaches for monitoring 8-day 30 m actual evapotranspiration. *ISPRS Journal of Photogrammetry and Remote Sensing* **126**, 79–93.

Kelliher, F. M., Leuning, R., Raupach, M. R. & Schulze, E. D. 1995 Maximum conductances for evaporation from global vegetation types. *Agricultural and Forest Meteorology* **73** (1–2), 1–16.

Khaniya, B., Priyantha, H. G., Baduge, N., Azamathulla, H. M. & Rathnayake, U. 2020 Impact of climate variability on hydropower generation: a case study from Sri Lanka. *ISH Journal of Hydraulic Engineering* **26** (3), 301–309.

Leuning, R., Zhang, Y. Q., Rajaud, A., Cleugh, H. & Tu, K. 2008 A simple surface conductance model to estimate regional evaporation using MODIS leaf area index and the penman-monteith equation. *Water Resources Research* **44** (10), No. W10419, 1–17.

Li, S., Kang, S., Zhang, L., Zhang, J., Du, T., Tong, L. & Ding, R. 2016 Evaluation of six potential evapotranspiration models for estimating crop potential and actual evapotranspiration in arid regions. *Journal of Hydrology* **543**, 450–461.

Minacapilli, M., Consoli, S., Vanella, D., Ciraolo, G. & Motisi, A. 2016 A time domain triangle method approach to estimate actual evapotranspiration: application in a Mediterranean region using MODIS and MSG-SEVIRI products. *Remote Sensing of Environment* **174**, 10–23. *Hydrology*, *543*, 450–461.

Mobilia, M. & Longobardi, A. 2021 Prediction of potential and actual evapotranspiration fluxes using six meteorological data-based approaches for a range of climate and land cover types. *ISPRS International Journal of Geo-Information* **10** (3), 192.

Morse, A., Tasumi, M., Allen, R. G. & Kramber, W. J. 2000 *Application of the SEBAL methodology for Estimating Consumptive Use of Water and Streamflow Depletion in the Bear River Basin of Idaho through Remote Sensing: Final Report*. Idaho Department of Water Resources, Idaho, pp. 1–107.

Mu, Q., Heinsch, F. A., Zhao, M. & Running, S. W. 2007 Development of a global evapotranspiration algorithm based on MODIS and global meteorology data. *Remote Sensing of Environment* **111** (4), 519–536.

Nagler, P. L., Cleverly, J., Glenn, E., Lampkin, D., Huete, A. & Wan, Z. 2005 Predicting riparian evapotranspiration from MODIS vegetation indices and meteorological data. *Remote Sensing of Environment* **94** (1), 17–30.

Richards, J. M. 1971 A simple expression for the saturation vapor pressure of water in the range −50 to 140 °C. *Journal of Physics D: Applied Physics* **4** (4), L15.

Ruhoff, A. L., Paz, A. R., Aragao, L. E. O. C., Mu, Q., Malhi, Y., Collischonn, W., Rocha, H. R. & Running, S. W. 2013 Assessment of the MODIS global evapotranspiration algorithm using eddy covariance measurements and hydrological modelling in the Rio Grande basin. *Hydrological Sciences Journal* **58** (8), 1658–1676.

Sugita, M. & Brutsaert, W. 1991 Daily evaporation over a region from lower boundary layer profiles measured with radiosondes. *Water Resources Research* **27**, 747–752.

Tasumi, M., Trezza, R., Allen, R. G. & Wright, J. L. 2003, September US Validation tests on the SEBAL model for evapotranspiration via satellite. In: *2003 ICID Workshop on Remote Sensing of ET for Large Regions*, Vol. 17.

Taylor, R. G., Scanlon, B., Döll, P., Rodell, M., Van Beek, R., Wada, Y., Longuevergne, L., Leblanc, M., Famiglietti, J. S., Edmunds, M. & Konikow, L. 2013 Ground water and climate change. *Nature climate change* **3** (4), 322–329. https://doi.org/10.1038/nclimate1744.

Zhang, Y. Q., Chiew, F. H. S., Zhang, L., Leuning, R. & Cleugh, H. A. 2008 Estimating catchment evaporation and runoff using MODIS leaf area index and the Penman-Monteith equation. *Water Resources Research* **44** (10), No. W10420, 1–15.

Zhang, X., Ren, Y., Yin, Z. Y., Lin, Z. & Zheng, D. 2009 Spatial and temporal variation patterns of reference evapotranspiration across the Qinghai-Tibetan Plateau during 1971–2004. *Journal of Geophysical Research Atmospheres* **114** (15), No. D15105, 1–14.

First received 13 September 2021; accepted in revised form 18 January 2022. Available online 2 February 2022